



This is a repository copy of *Construction of Zn-doped RuO₂ nanowires for efficient and stable water oxidation in acidic media*.

White Rose Research Online URL for this paper:

<https://eprints.whiterose.ac.uk/199026/>

Version: Published Version

Article:

Zhang, D. orcid.org/0000-0002-2124-3867, Li, M., Yong, X. orcid.org/0000-0003-1674-754X et al. (7 more authors) (2023) Construction of Zn-doped RuO₂ nanowires for efficient and stable water oxidation in acidic media. *Nature Communications*, 14 (1). 2517. ISSN 2041-1723

<https://doi.org/10.1038/s41467-023-38213-1>

Reuse

This article is distributed under the terms of the Creative Commons Attribution (CC BY) licence. This licence allows you to distribute, remix, tweak, and build upon the work, even commercially, as long as you credit the authors for the original work. More information and the full terms of the licence here:

<https://creativecommons.org/licenses/>

Takedown

If you consider content in White Rose Research Online to be in breach of UK law, please notify us by emailing eprints@whiterose.ac.uk including the URL of the record and the reason for the withdrawal request.



eprints@whiterose.ac.uk
<https://eprints.whiterose.ac.uk/>

Construction of Zn-doped RuO₂ nanowires for efficient and stable water oxidation in acidic media

Received: 15 October 2022

Accepted: 21 April 2023

Published online: 02 May 2023

Check for updates

Dafeng Zhang^{1,5}, Mengnan Li^{1,5}, Xue Yong^{2,3,5}, Haoqiang Song², Geoffrey I. N. Waterhouse⁴, Yunfei Yi¹, Bingjie Xue¹, Dongliang Zhang¹, Baozhong Liu¹✉ & Siyu Lu²✉

Oxygen evolution reaction catalysts capable of working efficiently in acidic media are highly demanded for the commercialization of proton exchange membrane water electrolysis. Herein, we report a Zn-doped RuO₂ nanowire array electrocatalyst with outstanding catalytic performance for the oxygen evolution reaction under acidic conditions. Overpotentials as low as 173, 304, and 373 mV are achieved at 10, 500, and 1000 mA cm⁻², respectively, with robust stability reaching to 1000 h at 10 mA cm⁻². Experimental and theoretical investigations establish a clear synergistic effect of Zn dopants and oxygen vacancies on regulating the binding configurations of oxygenated adsorbates on the active centers, which then enables an alternative Ru–Zn dual-site oxide path of the reaction. Due to the change of reaction pathways, the energy barrier of rate-determining step is reduced, and the over-oxidation of Ru active sites is alleviated. As a result, the catalytic activity and stability are significantly enhanced.

Hydrogen (H₂) generation via electrochemical water splitting is a promising way to efficiently store intermittent renewable energy^{1–3}. However, the sluggish oxygen evolution reaction (OER) on anode hinders the overall efficiency of water splitting and leads to large undesired energy consumption^{4,5}. Therefore, the design of high performance OER catalysts is regarded as a matter of urgency for the industrial application of water-to-H₂ conversion^{6–9}. To date, attractive candidates based on earth-abundant transition metals, especially the (oxy)hydroxides and layered double hydroxides of Ni–Fe^{10–12}, have been widely reported under basic conditions, offering a chance to build low-cost alkaline water electrolysis (AWE) assemblies without noble metals in application. However, the currently deployed AWE devices are still facing intrinsic challenges, including the low operating pressure, inevitable gas crossover, slow load response, and limited current density, mainly due to the utilization of a diaphragm and a liquid electrolyte¹³.

Compared with AWE, water electrolysis using proton exchange membrane (PEM) electrolyzers can effectively address the above challenges with significantly improved performance^{14–16}. But the highly corrosive conditions at high oxidation potentials under acidic environments make the development of efficient OER catalysts a great challenge. Most existing OER catalysts with excellent performance in basic condition generally show unsatisfied kinetics in acidic media, which, furthermore, suffer from severe degradation under the harsh conditions. So far, only the catalysts based on Ru and Ir noble metals can meet the requirements of PEM water electrolysis in practical deployment, though the scarcity of iridium and relatively low mass activity of Ir-based catalysts are serious obstacles to industrial scale H₂ production^{8,17,18}. Ru-based catalysts, especially RuO₂, show promise as OER catalysts in acidic media, being much cheaper than their Ir-based counterparts. The moderate binding strength of OER intermediates

¹State Collaborative Innovation Center of Coal Work Safety and Clean-efficiency Utilization, Henan Key Laboratory of Coal Green Conversion, College of Chemistry and Chemical Engineering, Henan Polytechnic University, Jiaozuo 454003, P. R. China. ²Green Catalysis Center, and College of Chemistry, Zhengzhou University, Zhengzhou 450000, P. R. China. ³Department of Chemistry, The University of Sheffield, Sheffield S3 7HF, UK. ⁴School of Chemical Sciences, The University of Auckland, Auckland 1142, New Zealand. ⁵These authors contributed equally: Dafeng Zhang, Mengnan Li, Xue Yong.

✉ e-mail: bzliu@hpu.edu.cn; sylu2013@zzu.edu.cn

(O*, OH*, and OOH*) on Ru sites makes Ru-based catalysts very active for oxygen evolution, but the over-oxidation of Ru cations can create soluble species (Ru^{n+} , $n > 4$) under acidic OER conditions, leading to rapid catalyst degradation and large losses in performance^{19–21}. Poor durability is the biggest obstacle hindering the practical application of Ru-based catalysts in PEM water electrolyzers^{22,23}.

Guest elements are usually introduced to improve the OER performance of RuO_2 by modulating the chemical environment of Ru centers²⁴. As reported recently, via constructing guest single atomic (e.g., Ni, Pt)^{25,26} and lattice doping (e.g., Mn, Cu, Na)^{27–29} sites, the overpotential of acidic OER on RuO_2 can be reduced to $-180 \text{ mV}@10 \text{ mA cm}^{-2}$ with a durability over 200 h²⁵. It was found that the presence of charge transfer between guest atoms and Ru cations can change the electronic structures of the Ru active sites^{30–33}. The introduction of electron-donating dopants into RuO_2 would reduce the oxidation state of Ru (Ru^{n+} , $n < 4$), thus protecting surface Ru cations from over oxidation to soluble species during OER^{34,35}. However, lowering the Ru oxidation state can impair the catalytic activity for OER, since the strong binding of OER intermediates on low-valent Ru sites would hinder the deprotonation of the second water molecule to form *OOH species³⁶. Thus, high-valent Ru species generally show faster kinetics with lower overpotentials during OER^{26,37,38}. The introduction of guest metal ions further provides a chance to create structure defects (e.g., oxygen vacancies, V_{O}) to modulate the OER property of Ru centers³¹. Although the presence of V_{O} defects would in principle reduce the oxidation state of Ru species and thus probably impair the OER activity^{37,39}, the possible synergy between V_{O} defects and guest elements would efficiently regulate the OER activity of Ru centers, which is not yet fully understood^{40–42}.

From a practical perspective, in addition to the intrinsic activity, the number of active sites is also important for improving OER performance. The number of active sites can be enhanced by increasing the surface area-to-mass ratio of catalysts via morphology engineering⁴³. RuO_2 -based materials with high aspect ratio morphologies demonstrate excellent activity for OER in acidic media^{32,44,45}. In order to improve the stability of RuO_2 -based OER catalysts, direct construction of high aspect ratio RuO_2 nanoarrays on conductive/corrosion resistant substrates is a preferred strategy. Additionally, close contact between the catalyst and substrate can also reduce interfacial charge transport resistance and facilitate the electron transfer for more efficient OER⁴⁶.

Inspired by the structural advantages of dimensionally stable anodes (DSA)⁴⁷, we herein synthesized Zn-doped RuO_2 (py- RuO_2 :Zn) nanowire arrays on Ti substrate using a simple pyrolysis method. The developed py- RuO_2 :Zn catalyst offered outstanding catalytic activity and stability for OER in acidic media (0.5 M H_2SO_4). RuO_2 doping by Zn^{2+} ions promoted the growth of nanowires (thereby increasing the availability of Ru active sites for OER), whilst also introducing V_{O} defects and low-valent Ru sites. Theoretic investigations revealed that V_{O} defects and Zn dopants caused a weakened binding of oxygen adsorbates at active Ru centers and, more interestingly, enable a moderate adsorption of *OH species on Zn sites. Consequently, a Ru–Zn dual-site oxide path of OER was favored and significantly enhanced the OER activity. In the meantime, the alternation of OER path avoided the over oxidation of the active metal centers, and the presence of Zn dopants and V_{O} defects enabled a structure stabilization of RuO_2 matrix. As a result, the py- RuO_2 :Zn nanowires exhibited low overpotentials for OER at current densities up to 1000 mA cm^{-2} , together with outstanding stability reaching 1000 h at 10 mA cm^{-2} , outperforming commercial RuO_2 and most recently reported RuO_2 -based catalysts.

Results and discussion

Preparation and characterization of py- RuO_2 :Zn

The py- RuO_2 :Zn nanowire arrays were fabricated by a straightforward pyrolysis method directly on a Ti plate (Fig. 1a), similar to the DSA

production in industrial applications⁴⁷. In brief, a certain volume of aqueous solution containing RuCl_3 and $\text{Zn}(\text{NO}_3)_2$ precursors (Zn/Ru atomic ratio = 0.5:1) was pipetted onto a freshly etched Ti plate over a confined rectangular area. After dried naturally at room temperature, the sample was then pyrolyzed at 350°C in air to transform the precursors into metal oxides. Finally, the undesired ZnO component in the product was removed by an acid etching treatment. The derived py- RuO_2 :Zn product appeared as a dark gray coating tightly adhered to the Ti substrate (Supplementary Fig. 1). Inductively coupled plasma mass spectrometry (ICP-MS) results reveal that about 10% of Ru and 90% of Zn were removed after the acid etching treatment, leading to a decrease in the Zn/Ru atomic ratio from 54.6% to 6.39% (Supplementary Table 1). This change was confirmed by an energy-dispersive X-ray spectroscopy (EDS) analysis, which shows a similar Zn/Ru decrease from 56.6% to 5.15%, with both elements uniformly dispersing in the etched coating (Supplementary Figs. 2–3). Mass loadings of Ru and Zn in the acid-etched py- RuO_2 :Zn coating are calculated to be 520.0 and $21.5 \mu\text{g cm}^{-2}$, respectively, according to the ICP-MS results.

Figure 1b shows a grazing incidence X-ray diffraction (GIXRD, incident angle 0.3°) pattern of the py- RuO_2 :Zn catalyst, as well as a pattern of the py- RuO_2 catalyst that was prepared following the same pyrolysis method in the absence of the zinc precursor. The diffraction peaks of py- RuO_2 :Zn were almost the same as those of py- RuO_2 , well matching the database pattern of rutile RuO_2 (JCPDS no. 43-1027). No peaks for ZnO were found. According to previous reports, Zn^{2+} prefers to substitutionally dope RuO_2 at Ru^{4+} sites^{30,48}, which is readily understood by the similar ionic radius of Ru^{4+} (0.62 \AA) and Zn^{2+} (0.60 \AA)⁴⁹. Zn-doped RuO_2 retains the rutile structure of pristine RuO_2 ⁴⁸, with negligible shift in the XRD peaks seen for py- RuO_2 :Zn due to the low Zn content ($<5 \text{ at.}\%$). However, the diffraction peaks for py- RuO_2 :Zn were much broader than those of py- RuO_2 (Fig. 1b), suggesting a decrease in the grain size resulting from Zn doping. The morphology of py- RuO_2 :Zn was next characterized by the scanning electron microscopy (SEM), with the analysis revealing a thin adherent coating with abundant microscale cracks from the precursor drying and pyrolysis steps (Fig. 1c and Supplementary Fig. 4). The coating contains dense arrays of high-quality nanowires with an average length of about 100 nm and a square cross-section along the growth direction (Fig. 1c (inset) and d–f). Control experiments revealed that the morphology of the nanowire arrays depended greatly on the composition and dosage of precursor solution and the pyrolysis temperature (Supplementary Figs. 5–7). In addition, the py- RuO_2 :Zn nanowire arrays could readily be fabricated on other substrates, such as carbon fiber paper (CFP) and fluorine-doped tin oxide (FTO) glass (Supplementary Fig. 8), highlighting the versatility of one-step pyrolysis catalyst fabrication strategy developed herein^{50–54}. But both CFP and FTO supported py- RuO_2 :Zn catalyst shows a relatively lower OER activity for acidic OER (Supplementary Fig. 8). Therefore, the Ti plate was selected as the support for py- RuO_2 :Zn catalyst in this work, which is a widely used DSA material in chlorine evolution process⁴⁷.

Transmission electron microscopy (TEM) analysis revealed that the nanowires had a length around 100 nm and an average diameter of 9.7 nm, corresponding to an aspect ratio (length/diameter) of ~ 10 (Fig. 1g). In the high-resolution TEM (HRTEM) images, random step and kink defects were found at the edges, possibly caused by the acid etching treatment (Fig. 1h). Lattice fringes with distinct interplanar distances of 3.20 \AA and 1.53 \AA were seen in the HRTEM images, well matching the (110) and (002) planes of rutile RuO_2 , respectively. This indicated that the nanowires were enclosed by {110} facets (Fig. 1i–j). The corresponding fast Fourier-transformation (FFT) electron diffraction pattern was in good agreement with the simulated one viewed along $[\bar{1}10]$ zone axis, suggesting single phase character and a [001] growth direction (*c*-axis) in the nanowire (Fig. 1i (inset) and j). The relative spatial distribution of Ru, Zn, and O elements in a single nanowire was studied by EDS under high-angle annular dark-field

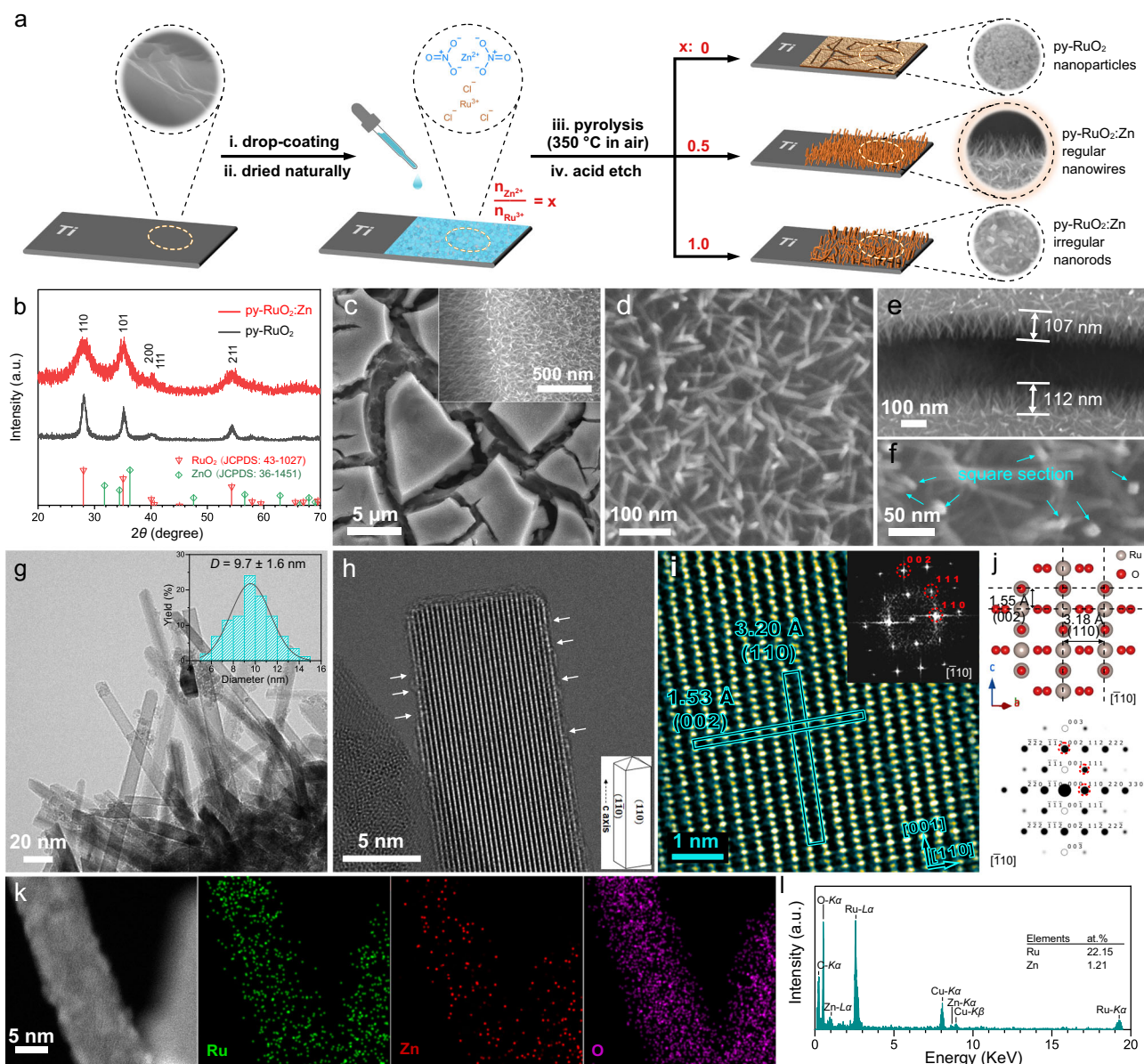


Fig. 1 | Preparation scheme and physical characterizations of py-RuO₂:Zn. **a** Schematic illustration of catalyst fabrication method. **b** XRD patterns of py-RuO₂:Zn and py-RuO₂ catalysts. **c, d** SEM images of py-RuO₂:Zn catalyst. **e** length and **f** section morphology analysis of nanowires. **g** TEM image and diameter distribution analysis (inset), and **h** HRTEM image (inset: illustration of the exposed

planes and growth direction) of nanowires. **i** HRTEM image and corresponding FFT pattern (inset), and **j** crystal structure simulation of the py-RuO₂:Zn catalyst. **k** HAADF-STEM images and **l** EDS analysis of Ru, Zn, and O elements in the py-RuO₂:Zn catalyst.

scanning TEM (HAADF-STEM) mode. As shown in Fig. 1k and l, each element was uniformly dispersed throughout the nanowire with a Zn/Ru atom ratio of 5.46%. This value is very close to those obtained from the ICP-MS and SEM-EDS studies (Supplementary Table 1). Interstitial Zn dopants were not seen in the atomic-resolution TEM image of a nanowire (Fig. 1i), confirming substitutional Zn doping and consistent with the XRD results.

The surface chemical information of py-RuO₂:Zn and two pure RuO₂ catalysts were next investigated by X-ray photoelectron spectroscopy (XPS). The Survey XPS spectrum confirmed the presence of Zn in py-RuO₂:Zn (Supplementary Fig. 9), while the core-level Zn 2p spectrum showing peaks at 1021.4 and 1044.3 eV in a 2:1 area ratio which could readily be assigned to the Zn 2p_{3/2} and Zn 2p_{1/2} signals, respectively, of Zn²⁺ species (Supplementary Fig. 10)^{55–57}. The Ru 3d XPS spectrum for py-RuO₂:Zn showed intense peaks at -281.0 and 285.0 eV (3:2 area ratio), which could readily be assigned to the 3d_{5/2}

and 3d_{3/2} orbitals, respectively, of Ru⁴⁺ in RuO₂ (Supplementary Fig. 11)^{32,58}. Corresponding Ru⁴⁺ shake-up satellites were seen at -283.1 and 287.2 eV, with the C 1s peak of adventitious hydrocarbons being buried under the Ru 3d signal. The Ru 3d peaks for py-RuO₂:Zn and py-RuO₂ were positively shifted by about 0.3–0.4 eV compared with data for the commercial RuO₂ powder catalyst (c-RuO₂), indicating a variation of the local chemical environment at Ru sites (possibly originating from particle size effects)^{58,59}. Peaks in less intensity were further observed at -282.0 and 286.2 eV, assigned to the 3d_{5/2} and 3d_{3/2} orbitals, respectively, of Ru³⁺ in RuO₂⁵⁸. The abnormally positive shifts in binding energies are caused by the coordination with hydroxyl adsorbates^{58,60}. In fact, non-stoichiometric Ru³⁺ species generally exist in RuO₂ films prepared by thermal decomposition of RuCl₃ precursors^{61,62}. The Ru 3p_{3/2} spectra for the different catalysts showed a main peak at 462.9 eV confirmed the predominance of Ru⁴⁺ species in all samples (Fig. 2a and Supplementary Fig. 12)^{45,58,59}. A weak peak at

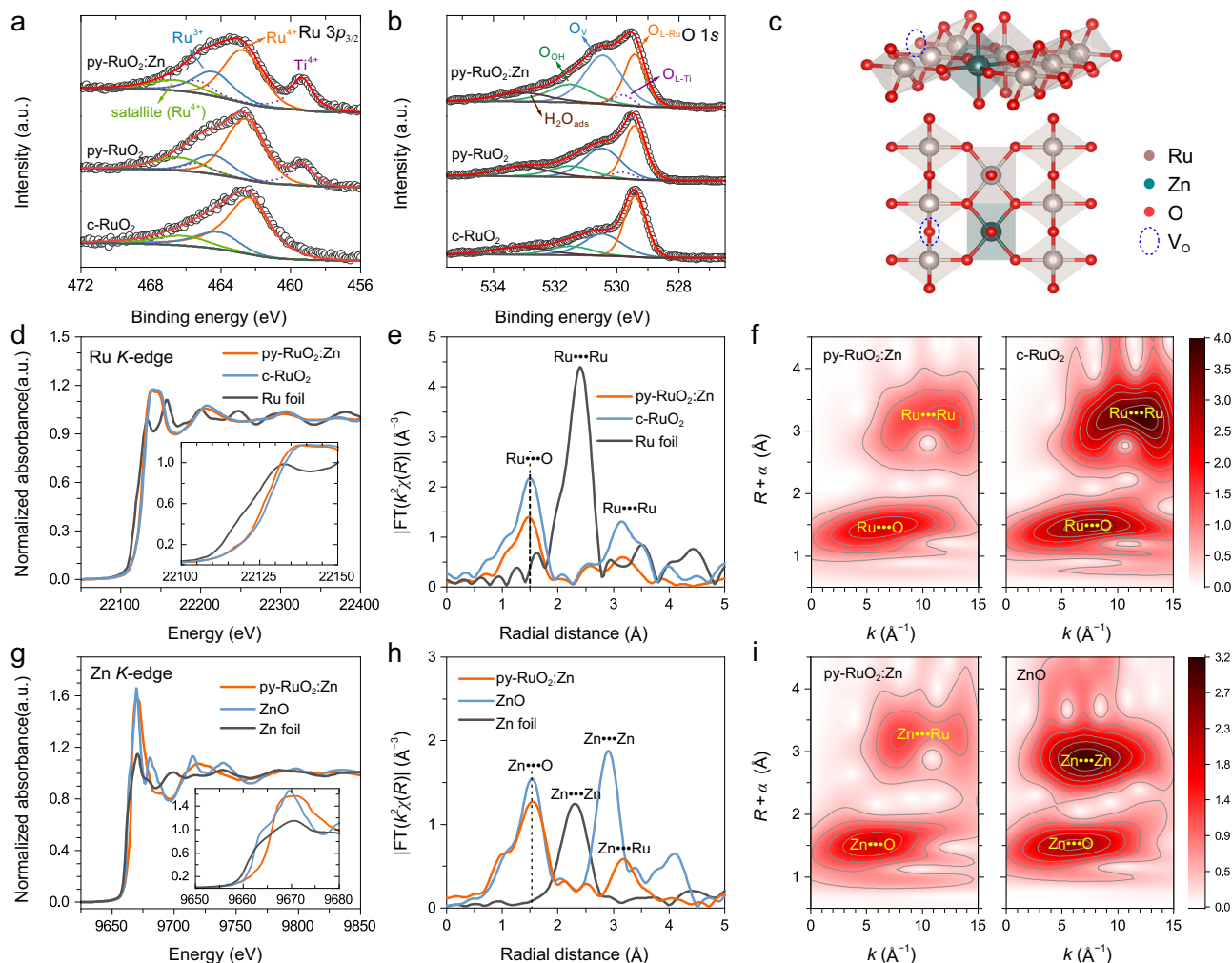


Fig. 2 | XPS and XAS characterizations of py-RuO₂:Zn. **a** Ru 3p_{3/2} and **b** O 1s core level XPS spectra for the py-RuO₂:Zn, py-RuO₂, and c-RuO₂ catalysts. **c** Simulated structure of the py-RuO₂:Zn catalyst. **d** Normalized Ru K-edge XANES and **e** Ru K-edge FT-EXAFS spectra of py-RuO₂:Zn, c-RuO₂, and Ru foil. **f** Ru K-edge WT-EXAFS spectra of py-RuO₂:Zn and c-RuO₂. **g** Normalized Zn K-edge XANES and **h** Zn K-edge FT-EXAFS spectra of py-RuO₂:Zn, ZnO, and Zn foil. **i** Zn K-edge WT-EXAFS spectra of py-RuO₂:Zn and ZnO.

464.7 eV showed the presence of some Ru³⁺ species^{58,60}. The integrated area of the Ru³⁺/Ru⁴⁺ signals was then calculated to examine the relative abundance of Ru³⁺ in the different catalysts. As shown in Supplementary Table 2, the Ru³⁺/Ru⁴⁺ ratio was similar for c-RuO₂ (0.25) and py-RuO₂ (0.31), but increased considerably on going to py-RuO₂:Zn (0.55), suggesting that Zn doping increased the concentration of Ru³⁺ species. The higher content of low-valent Ru species on the surface of py-RuO₂:Zn catalyst remained under the OER conditions, as confirmed by the Raman measurements (Supplementary Fig. 13). Since the TEM data in Fig. 1i confirmed the presence of the rutile phase in py-RuO₂:Zn, a higher Ru³⁺ concentration suggested abundant oxygen vacancy (V_O) defects in the catalyst. The O 1s XPS spectra validated this hypothesis. As shown in Fig. 2b, the O 1s spectra showed peaks below 530.0 eV due to lattice oxygen of RuO₂ (O_{L-Ru}) and TiO₂ (O_{L-Ti}, from the thin oxide layer on the Ti substrate in cracked areas of the film), and the peaks at 530.5, 531.5, and 533.0 eV due to O atoms in the vicinity of V_O defect (O_V), chemisorbed hydroxyl groups (O_{OH}), and surface-adsorbed H₂O (H₂O_{ads}), respectively^{63–65}. Clearly, the intensity of O_V peak increased on going from pure c-RuO₂ to py-RuO₂:Zn. The O_V/O_{L-Ru} ratio on py-RuO₂:Zn (1.63) was more than twice that of c-RuO₂ (0.67) (Supplementary Table 2). Good linear relationships were further recognized between the concentrations of O_V and O_{OH} and the abundance of Ru³⁺ species (Supplementary Fig. 14), again proving the change in the

coordination of Ru sites in the catalyst. In summary, the XPS results reveal that Zn doping caused more low-valent Ru³⁺ species and V_O defects in the RuO₂ structure, both of which would impact the activity and durability of RuO₂-based catalysts for acidic OER^{33,42}.

XPS probes the top few nanometers in materials. To gain more comprehensive insights about the bulk electronic structure of the py-RuO₂:Zn catalysts, we carried out X-ray absorption spectroscopy (XAS) measurements at the Ru K-edge and Zn K-edge. Figure 2d shows Ru K-edge X-ray absorption near-edge structure (XANES) spectra for py-RuO₂:Zn, Ru metal foil, and pure RuO₂ powder. The absorption edge positions for py-RuO₂:Zn and RuO₂ were at higher energy compared to that of the Ru foils, reflecting the higher oxidation state of Ru in the oxide materials. The absorption edge of py-RuO₂:Zn was at slightly lower energy than for the c-RuO₂, suggesting a slightly lower Ru valence state in py-RuO₂:Zn. Calculations on basis of adsorption edge energy revealed that an average oxidation state of Ru species in the catalyst was approximately +3.4 (Supplementary Fig. 15), which was considered as the combination of pristine Ru⁴⁺ and Ru³⁺ cations. The Zn K-edge XANES spectra for py-RuO₂:Zn, ZnO powder, and Zn foil are shown in Fig. 2g. The spectrum for py-RuO₂:Zn was quite distinct to those of the references samples, revealing a Zn²⁺ oxidation state but without the fine structure associated with ZnO. The “white line” feature of py-RuO₂:Zn was considerably broader than that of the bulk ZnO

reference and did not show the characteristic ZnO shoulder at $-9663 \text{ eV}^{66,67}$. The results indicate that the coordination of Zn^{2+} atoms in py-RuO₂:Zn was different to the tetrahedral Zn–O coordination found in wurtzite ZnO, with the obvious explanation being the adoption of an octahedral structure through substitutional doping of Zn at Ru sites in the RuO₂ lattice^{66,67}.

We note that when the Zn dopants took an octahedral coordination structure through substitutionally doping at Ru sites in the RuO₂ lattice, a fraction of the Ru will, in principle, be oxidized above +4 to accommodate the divalent metal, associated with a generation of stoichiometric oxide³⁰. However, when oxygen vacancies (V_{O}) present, the oxidation state of Ru^{n+} ($n > 4$) would be reduced. Recently, Liu and colleagues reported a Na-doped amorphous/crystalline RuO₂ catalyst containing more low-valent Ru^{n+} ($n < 4$) species with the presence of high abundant V_{O} defects⁴⁰. To further understand the role of Zn doping on the generation of V_{O} defects, the relationship between Zn content and V_{O} concentration was analyzed on basis of XPS results. A linear dependence of $O_{\text{V}}/O_{\text{L-Ru}}$ on the Zn content was found (Supplementary Fig. 16), indicating that the doping of Zn element can induce the generation of V_{O} defects. In the meantime, the presence of Ru^{3+} and V_{O} defects was also found in the undoped py-RuO₂ catalyst, seemingly caused by the catalyst synthesis method used here^{61,62}. Thus, it can conclude that the Zn doping, in addition to the catalysis synthesis method, has induced the generation of V_{O} defects and the low-valent Ru sites.

Figure 2e shows Fourier transformed (FT) k^2 -weighted Ru K -edge extended X-ray absorption fine structure (EXAFS) spectra for py-RuO₂:Zn and relevant reference samples. The main peaks at 1.50 and 3.14 Å for pure RuO₂ correspond to the first Ru–O and Ru–Ru coordination shells of Ru cations^{31,68}, respectively. For py-RuO₂:Zn, these sample features were observed at 1.47 and 3.17 Å, respectively, indicating a slight change in Ru cation coordination environment with Zn doping. Compared with RuO₂, py-RuO₂:Zn showed reduced intensities for both Ru–O and Ru–Ru peaks, suggesting that the coordination number of Ru sites was decreased⁶⁹, consistent with the presence of V_{O} defects. Further, the substitutionally doping of Zn would make the second peak a mixture of Ru–Ru and Ru–Zn scattering. In addition, the Zn K -edge EXAFS spectrum of py-RuO₂:Zn in Fig. 2h closely resembled the Ru K -edge spectrum, suggesting an octahedral-like Zn coordination (Supplementary Fig. 17). The first peak observed at 1.55 Å in the Zn K -edge R -space plot for py-RuO₂:Zn, assigned to the first Zn–O coordination shell, was longer than the 1.47 Å for Ru–O bonds (as expected since Zn^{2+} has a lower charge than Ru^{4+}). The second strong peak at 3.18 Å was longer than the Zn–Zn shell distance in ZnO (2.91 Å), being more comparable to the Ru–Ru distance (3.17 Å) in py-RuO₂:Zn or c-RuO₂ (3.14 Å). Previously, Petrykin and colleagues reported similar Zn K -edge EXAFS spectra for $\text{Ru}_{1-x}\text{Zn}_x\text{O}_2$ ($x \leq 0.2$) materials and assigned the peak located at -3.1 \AA to Zn–Ru backscattering at Zn sites based on a structural fitting analysis⁴⁸. We believe, the peak at 3.18 Å in the Zn K -edge spectrum of py-RuO₂:Zn has the same origin, arising from substitution of Ru ions by Zn ions in the py-RuO₂:Zn catalyst. The wavelet transform (WT) EXAFS measurements provided further confirmation for this assignment (Fig. 2f and i, and Supplementary Fig. 18). The maximum-intensity Ru K -edge values for py-RuO₂:Zn were observed at $k \approx 6.5$ and 12.5 \AA^{-1} , attributed to Ru–O and Ru–Ru/Zn scattering paths (Fig. 2f), respectively. These features were weaker than those of the reference RuO₂ sample, which may have been due to the nanosize of the py-RuO₂:Zn nanowires and also the mixed Ru–Ru/Zn coordination shell. The Zn K -edge WT plot of py-RuO₂:Zn in Fig. 2i showed a similar contour profile to the Ru K -edge plot in Fig. 2f. On basis of the observations, the model crystal structure for py-RuO₂:Zn could be proposed (Fig. 2c) based on the rutile structure of pure RuO₂ with partial substitution of Ru atoms by Zn atoms. The introduction of Zn^{2+} ions promotes the formation of oxygen vacancies in the near vicinity. The loss of O at the vertex of the RuO₆ octahedra would lower

the average Ru valence, which has particular relevance to the OER performance^{33,68}.

Electrocatalytic performance of py-RuO₂:Zn toward acidic OER

The OER activity of the as-prepared py-RuO₂:Zn catalyst was examined in an O₂-saturated 0.5 M H₂SO₄ electrolyte using a conventional three-electrode set-up. The Ag/AgCl reference electrode was first calibrated against the reversible hydrogen electrode (RHE) (Supplementary Fig. 19). For comparison, the activities of py-RuO₂ and c-RuO₂ were also measured under identical conditions. In order to minimize the background capacitive current, the linear sweep voltammetry (LSV) curves reported were obtained by taking the average results of the positive/negative-going scans of a cyclic voltammetry curve (CV) (Supplementary Fig. 20a). The capacitance-corrected LSV curve was then performed an 85% iR -compensation correction (Supplementary Fig. 20b)⁷⁰. The CV curves shows no obvious degradation during the first 30 cycles on py-RuO₂:Zn (Supplementary Fig. 21), implying that the pristine surface offered high OER activity without the need for pre-activation treatment⁷¹. Figure 3a displays the LSV results of OER on the different catalysts. The sharply rising anodic current related to the OER process appeared at more negative potentials on py-RuO₂:Zn compared to pure c-RuO₂. The associated OER onset potential was -1.33 V (vs RHE), corresponding to an overpotential (η) of -100 mV , much lower than those of py-RuO₂ (-1.38 V , $\eta \approx 150 \text{ mV}$) and c-RuO₂ (-1.42 V , $\eta \approx 190 \text{ mV}$) (Supplementary Fig. 22)⁷². Accordingly, the OER process is a more easily triggered on py-RuO₂:Zn. The superior OER activity of py-RuO₂:Zn was retained on increasing the current density. To achieve a current density of 10 mA cm^{-2} , py-RuO₂:Zn required a low potential of 1.403 V ($\eta = 173 \text{ mV}$), outperforming py-RuO₂ (1.458 V , $\eta = 228 \text{ mV}$) and the commercial c-RuO₂ reference catalyst (1.521 V , $\eta = 291 \text{ mV}$)^{40,73}. At a higher overpotential of $\eta = 300 \text{ mV}$, py-RuO₂:Zn achieves a current density of 476 mA cm^{-2} , which was 4.4 and 36.1 times as larger than values for py-RuO₂ and c-RuO₂, respectively (Fig. 3c). Moreover, the OER process can be polarized to an industrial current density of 1.0 A cm^{-2} on py-RuO₂:Zn catalyst, operating at a very competitive potential of 1.603 V ($\eta = 373 \text{ mV}$) (Fig. 3b)^{33,73}. Such a large current density can be reached more than five continuous CV cycles, but accompanied by a gradually degradation in the OER activity (Supplementary Fig. 23). The faradaic efficiency (FE) of OER on py-RuO₂:Zn catalyst was measured by the water displacement method under the chronopotentiometric condition at current densities of 25 and 40 mA cm^{-2} . As shown in Supplementary Fig. 24, the measured oxygen amount fits well with the theoretical values calculated from Faraday's law of electrolysis, approaching $\sim 99\%$ and $\sim 100\%$ FE at 25 and 40 mA cm^{-2} , respectively. Notably, the OER activity of py-RuO₂:Zn was greatly affected by the conditions of catalyst preparation (Supplementary Figs. 5–7), with the optimal OER performance being achieved with a regular nanowire morphology on Ti plate.

To evaluate the intrinsic OER performance of the py-RuO₂:Zn catalyst, we further calculated the mass activity according to the total loading of Ru metal determined by ICP-MS (Supplementary Table 1). As shown in Fig. 3a, the OER mass activity of the py-RuO₂:Zn catalyst greatly surpassed those of py-RuO₂ and c-RuO₂. A current density of $100 \text{ mA mg}_{\text{Ru}}^{-1}$ can be achieved at a low potential of 1.442 V ($\eta = 212 \text{ mV}$) on py-RuO₂:Zn, whereas 1.508 V ($\eta = 278 \text{ mV}$) and 1.607 V ($\eta = 377 \text{ mV}$) were required on py-RuO₂ and c-RuO₂, respectively. At $\eta = 300 \text{ mV}$, py-RuO₂:Zn delivered a current density up to $881 \text{ mA mg}_{\text{Ru}}^{-1}$ (Fig. 3c). In contrast, just $181 \text{ mA mg}_{\text{Ru}}^{-1}$ was realized on py-RuO₂ and $22.0 \text{ mA mg}_{\text{Ru}}^{-1}$ on c-RuO₂⁷³. The remarkable OER activity of the py-RuO₂:Zn catalyst well retained at high current densities, evidenced by values of $1.538 \text{ V}@1.0 \text{ A mg}_{\text{Ru}}^{-1}$ and $1.611 \text{ V}@2.0 \text{ A mg}_{\text{Ru}}^{-1}$ (Fig. 3b). It is also worth noting that the OER activity of py-RuO₂:Zn greatly surpassed those of reported Zn-doped RuO₂ catalysts^{30,48,74}. A rutile-type $\text{Zn}_{0.19}\text{Ru}_{0.81}\text{O}_2$ was previously studied by Burnett and colleagues³⁰. Although the $\text{Zn}_{0.19}\text{Ru}_{0.81}\text{O}_2$ catalyst reported in that work displayed an OER activity

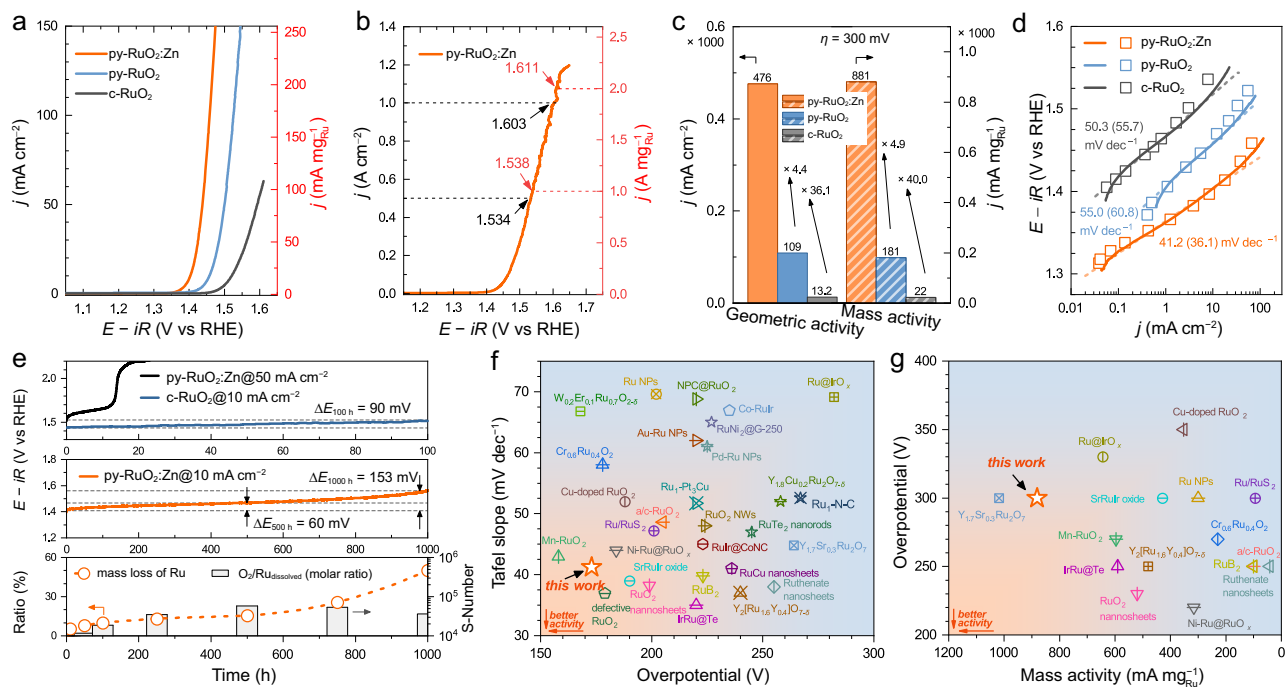


Fig. 3 | OER performance of py-RuO₂:Zn in acidic media. **a** Geometric area and Ru mass normalized LSV curves with 85% *iR*-correction of py-RuO₂:Zn, py-RuO₂, and c-RuO₂ for OER in 0.5 M H₂SO₄ solution (pH = 0.30 ± 0.01) with O₂ saturation. Solution resistances for *iR*-correction are 2.8, 2.6, and 4.5 Ω for py-RuO₂:Zn, py-RuO₂, and c-RuO₂, respectively. Mass loadings of Ru metal are 0.52, 0.60, and 0.60 mg cm⁻² for py-RuO₂:Zn, py-RuO₂, and c-RuO₂, respectively. **b** Geometric area and Ru mass normalized LSV curve of py-RuO₂:Zn for OER under high current density. **c** Comparisons of OER geometric and mass activities at an overpotential of 300 mV on py-RuO₂:Zn, py-RuO₂, and c-RuO₂. **d** Tafel plots derived from the LSV

curves (solid line) and the steady-state polarization curves (scatters). Values in parentheses were derived from steady-state polarization curves. **e** Chronopotentiometric stability tests of py-RuO₂:Zn and c-RuO₂ (upper plot: 100 h at 50 mA cm⁻²; middle plot: 1000 h at 10 mA cm⁻²) and mass loss analysis of Ru and corresponding stability number (S-Number) on py-RuO₂:Zn during the stability test determined by ICP-MS (lower plot). Comparison of overpotentials and **f** Tafel slopes, and **g** mass activities for py-RuO₂:Zn and other recently reported high performance RuO₂-based OER catalysts.

better than commercial RuO₂, its performance was vastly inferior to the py-RuO₂:Zn catalyst in the current study, with OER activity at $\eta = 300$ mV only reached at 60 mA mg_{Ru}⁻¹. Actually, Zn_{0.19}Ru_{0.81}O₂ was reported to possess a defect-free stoichiometric oxide. The fully occupied oxygen sites were proposed to require a higher average Ru oxidation state (above +4) to balance charge, which is obviously different to the structure of the defective py-RuO₂:Zn catalyst. The difference in crystal structure of the Zn-doped RuO₂ catalysts explains the variation in OER performance between our work and that of Burnett and colleagues³⁰. Recently, a surface evolution of Zn-doped RuO₂ under the reaction was found to enable a construction of surface defects (e.g., V_O defects) and active Ru sites⁷⁵, consistent with the theoretically predicted results on RuO₂ catalyst³⁹. A low overpotential of 190 mV and a good stability up to 60 h were observed at the current density of 10 mA cm⁻² on this surface etched catalyst. Next, the electrochemical active surface area (ECSA) was calculated for the different catalysts and used to normalize the OER current, in order to eliminate the effect of catalyst morphology. As shown in Supplementary Fig. 25, py-RuO₂:Zn possessed a much larger ECSA and a higher specific OER activity compared to the pure RuO₂ catalysts studied in this work, largely due to the significant difference in the morphology of them (Supplementary Fig. 5). Figure 3d shows the Tafel slope analyses for the different catalysts. The plots were derived from the *iR*-corrected LSV curves and the steady-state polarization curves (Supplementary Fig. 26)⁷⁶. Clearly, py-RuO₂:Zn offered the lowest Tafel slope of 41.2 (36.1) mV dec⁻¹, suggesting faster OER kinetics compared to the py-RuO₂ and c-RuO₂ catalysts^{25,73}. A Tafel slope around 40 mV dec⁻¹ implies a better kinetics of the OH_{ads} deprotonation to form O_{ads} and the O–O bond formation^{8,77}. Moreover, electrochemical impedance spectroscopy (EIS) results (Supplementary Figs. 27–28, and

Supplementary Table 3) showed that the charge transfer resistance (*R*_{ct}) was significantly smaller on py-RuO₂:Zn than it on pure py-RuO₂, for instance, 9.0 Ω and 114.7 Ω at 1.40 V, respectively, further proving a much faster charge transfer rate of OER and thereby an improved reaction kinetics on py-RuO₂:Zn. In summary, the py-RuO₂:Zn catalyst demonstrated excellent OER activity compared to the pure RuO₂ reference catalysts and state-of-the-art performance compared to RuO₂-based acidic OER catalysts recently reported (Fig. 3f, g, and Supplementary Table 4).

Next, catalytic stability of py-RuO₂:Zn during OER was investigated using a chronopotentiometric (CP) method at a constant current density. As shown in Fig. 3e, py-RuO₂:Zn displayed far better stability than the c-RuO₂ catalyst. At a typical current density of 10 mA cm⁻², the OER potential on py-RuO₂:Zn increased by only 60 mV during the initial 500 h of testing and by only 153 mV over 1000 h of testing. In contrast, the c-RuO₂ catalyst dramatically lost activity over 15 h under identical conditions^{41,73}. At a higher current density of 50 mA cm⁻², py-RuO₂:Zn showed excellent stability over 100 h with an overpotential increase of only 90 mV (Fig. 3e), while potential increase was 70 mV after a test at the current density of 100 mA cm⁻² for 24 h (Supplementary Fig. 29). The good stability of py-RuO₂:Zn was further investigated under the CV cycling condition. The potential at 100 mA cm⁻² was increased by about 28 mV after a 2000-cycles test (Supplementary Fig. 30). Compared with recently reported RuO₂-based catalysts, the stability of py-RuO₂:Zn was also more distinguished (Supplementary Table 4). For example, the degradation of the OER overpotential (ΔE) at 10 mA cm⁻² for py-RuO₂:Zn was much smaller than that reported for the best Ru/ α -MnO₂ ($\Delta E = 169$ mV@200 h) and Li₂RuO₂ ($\Delta E = 120$ mV@70 h) catalysts under similar testing conditions^{35,41}. During the stability test, the dissolution of Ru from py-RuO₂:Zn catalyst was

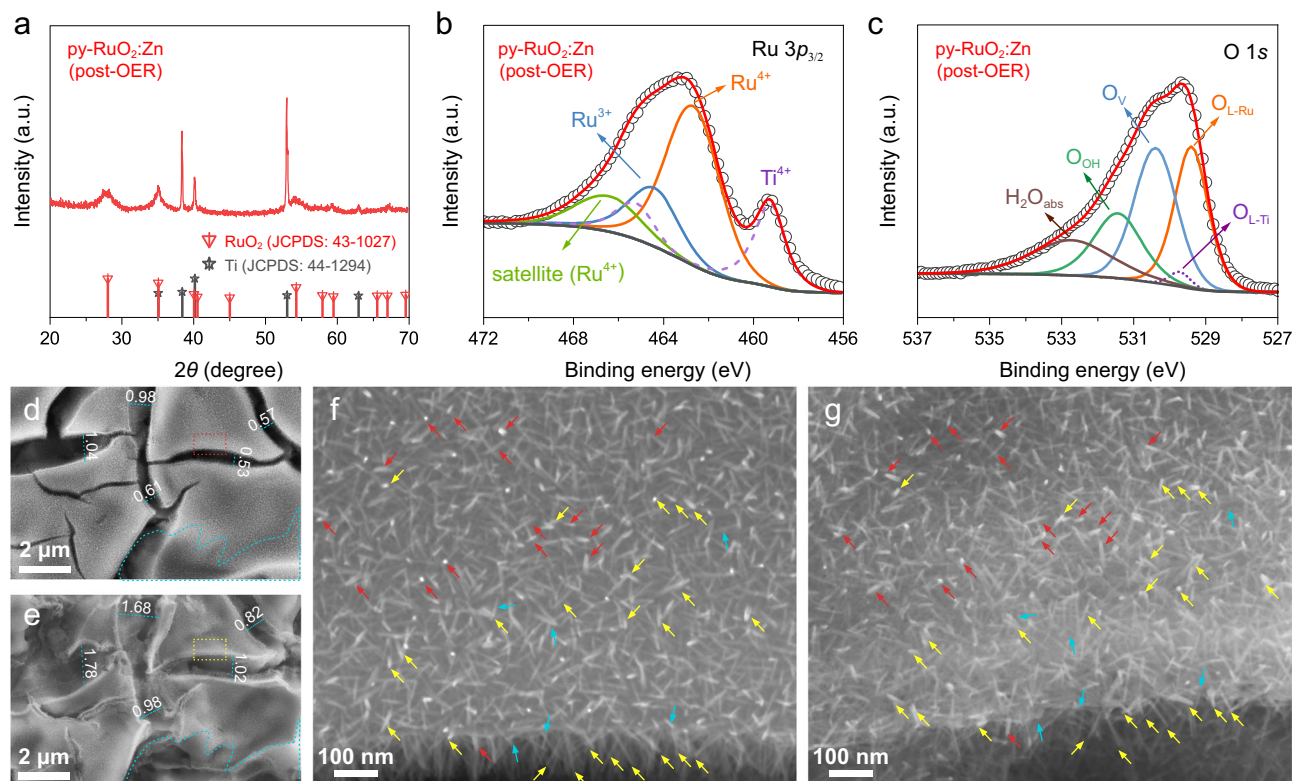


Fig. 4 | Stability analysis of py-RuO₂:Zn for acidic OER. **a** XRD pattern, **b** Ru 3p_{3/2} and **c** O 1s XPS spectra of py-RuO₂:Zn catalyst post OER test. Quasi-in situ SEM images of the py-RuO₂:Zn catalyst **d**, **f** before and **e**, **g** after a continuous OER test at

10 mA cm⁻² for 350 h. The red and yellow arrows indicate nanowires that retained or slightly lost their morphologies during OER, respectively, whilst the cyan arrows indicate nanowires that completely disappeared after the test.

determined by ICP-MS. Figure 3e (lower plot) shows the mass loss of Ru normalized against the initial Ru loading in freshly prepared py-RuO₂:Zn. Three distinct stages were seen in the Ru dissolution profile. During the initial 100 h, -10% Ru loss occurred with the loss increasing slowly to -15% after 500 h. In the final 1000 h, the Ru loss increased to -50%. This trend is generally consistent with the performance degradation behavior seen for the py-RuO₂:Zn catalyst in the CP stability test (Fig. 3e, middle plot). The OER potential shows an increase of 28 mV, from 1.408 V to 1.436 V, in the first 100 h test, followed by a further 32 mV increase from 1.436 V to 1.468 V between 100 h and 500 h. Finally, a larger 93 mV increase, from 1.468 V to 1.561 V, was found between 500 h and 1000 h. Consequently, although the OER potential degradation of py-RuO₂:Zn was very modest over 1000 h (compared to previously reported RuO₂ catalysts in acidic media), the -50% Ru mass loss at the end of the tests indicated serious corrosion in the latter stages, which was then confirmed by post-stability test SEM imaging and optical photographs (Supplementary Fig. 31). In addition, stability number (S-number), a recommended metric to quantify the catalyst stability during the reaction⁷⁸, was calculated by normalizing the moles of O₂ evolved ($n_{\text{O}_2, \text{evolved}}$) with the moles of Ru dissolved ($n_{\text{Ru dissolved}}$), i.e., $S\text{-number} = n_{\text{O}_2, \text{evolved}} / n_{\text{Ru dissolved}}$ ³⁸. As shown in Fig. 3e lower plot, the S-number exhibited an increase in the initial 500 h and then a decrease in the following 500 h. A top value of $\sim 6 \times 10^4$ was obtained, which is comparable to those observed on Ru-based pyrochlores³⁸. We also note that the mass loss of Ru up to -15% within 500 h from the py-RuO₂:Zn catalyst seems to be serious for industrial applications. However, the corresponding dissolution rate of Ru, $0.156 \mu\text{g cm}^{-2}_{\text{geo}} \text{h}^{-1}$, is much lower than that of the commercial RuO₂ ($\sim 40 \mu\text{g cm}^{-2}_{\text{geo}} \text{h}^{-1}$). Further compared with the high active RuO₂-based acidic OER catalysts recently reported (Supplementary Table 5), the py-RuO₂:Zn catalyst also ranks the top-level of stability in terms of the Ru dissolution rate. When normalized by the ECSA, a value of

$37.6 \text{ pg cm}^{-2}_{\text{ECSA}} \text{h}^{-1}$ for Ru dissolution rate was obtained on the py-RuO₂:Zn catalyst, significantly lower than the $\sim 1.05 \mu\text{g cm}^{-2}_{\text{ECSA}} \text{h}^{-1}$ on commercial RuO₂, indicating an intrinsically improved stability of the catalyst.

In order to gain deeper insights about py-RuO₂:Zn catalyst degradation during acidic OER, we performed a further durability test at 10 mA cm⁻² for 350 h (Supplementary Fig. 32). The 350 h was selected on basis of the apparent inflection point in the Ru dissolution curve (Fig. 3e, lower plot). XRD revealed that the py-RuO₂:Zn catalyst retained a rutile structure after 350 h (Fig. 4a). The core level Ru 3d, Ru 3p_{3/2}, and O 1s XPS spectra showed a slight decrease in the concentrations of Ru³⁺ species and V_O defects on the surface (Fig. 4b, c, Supplementary Fig. 33, and Supplementary Table 2). No obvious change was found in the Zn 2p XPS spectra (Supplementary Fig. 34). Quasi-in situ SEM measurements taken at some pre-marked locations before and after the OER stability test were used to study Ru dissolution from the py-RuO₂:Zn catalyst. Some corrosion was observed in the catalyst coating on the Ti plate after the test (Supplementary Fig. 35), accompanied by an expansion of the original coating cracks (Fig. 4d–e). The corrosion appears to begin preferentially at the edges of the cracks and then gradually expand into the plateau domains. A close comparison (marked by arrows) revealed that the majority of py-RuO₂:Zn nanowires retained their original locations and morphologies (marked by red arrows), especially those far from the cracks. Nanowires near the cracks showed more obvious changes in their spatial directions and morphologies (marked by yellow arrows). A few nanowires disappeared completely after the 350 h of testing (marked by cyan arrows). Optical images (Supplementary Fig. 31c) revealed that the py-RuO₂:Zn coating remained in a good condition after the 350 h test, showing good adhesion and a uniform dispersion of elements (Supplementary Fig. 36), which is consistent with a relatively slow mass loss of Ru during the first 500 h of OER testing (Fig. 3e, lower plot).

Results suggest that there is likely a threshold potential that determines the dissolution rate of Ru in the py-RuO₂:Zn catalyst during OER, above which dissolution proceeds very rapidly. Based on the CP results, this threshold potential appears to be -1.46 V (Supplementary Fig. 37). Anodic polarization higher than 1.46 V will result in accelerated corrosion of the py-RuO₂:Zn catalyst. The accelerated degradation of py-RuO₂:Zn at potentials above 1.46 V was further observed under a CP test at 100 mA cm⁻², which exhibited a faster increase of overpotential by 70 mV within 24 h (Supplementary Fig. 29). The result agrees with the previous reports on the stability window of RuO₂-based catalysts^{6,79,80}. Although the stability of py-RuO₂:Zn did not obviously break the reported potential limit, the onset overpotential of OER was significantly reduced, providing a widened stability window to the application of py-RuO₂:Zn. Furthermore, we find that the potential of 1.46 V is close to the inflection region in the Tafel plot (Supplementary Fig. 38), indicating a change in the rate-determining step of OER with the change in Ru dissolution rate^{8,77}.

Insights into OER process and relevant mechanism

On the LSV curve for OER (Fig. 3a and Supplementary Fig. 22), low onset potential (-1.33 V) and overpotential (173 mV at 10 mA cm⁻²) were observed and have been assigned to an anodic OER process on the py-RuO₂:Zn catalyst. Such low threshold potentials are impressive because they well exceeded the theoretical limit of OER onset overpotential (-250 mV) on the optimal catalyst, based on the adsorbate evolution mechanism (AEM) involving single active metal site and the linear scaling relationships between the adsorption energies of *O, *OH, and *OOH intermediates ($\Delta E_{\text{OOH}} = \Delta E_{\text{OH}} + 3.2 \text{ eV} \pm 0.2 \text{ eV}$)^{36,81}. We then performed experiments using a rotating ring-disk electrode (RRDE) setup and confirmed the explicit contribution of OER process to the observed anodic current at potentials around 1.40 V (Supplementary Fig. 39). Thus, the low threshold potentials of OER suggested that there may be other paths of OER on the py-RuO₂:Zn catalyst in addition to the AEM, especially at low overpotentials. Recently, Scott and colleagues performed a trace detection of O₂ and found an electrochemical generation of O₂ from OER on the RuO_x catalyst at the potential as low as 1.30 V⁸². Further by comparing the trends in Ru dissolution and oxygen evolution, they suggested a negligible contribution of lattice oxygen evolution to the overall OER activity for RuO_x in acidic media²². A comprehensive theoretical study on the recently reported mechanisms of OER revealed that the presence of nonelectrochemical steps (e.g., *OO dimer formation/desorption) tends to increase rather than to reduce the thermodynamic overpotential of OER, while the presence of surface defects (e.g., V_O defects) probably alters the configuration of adsorbed intermediates to improve the OER activity⁸³.

In this work, a high concentration of V_O defects and low-valent Ru species existed in the py-RuO₂:Zn catalyst, which may play important roles in improving the OER property^{31,41}, in addition to the catalyst electrical conductivity (Supplementary Fig. 28 and Supplementary Table 3)⁸⁴. When plotting specific current densities against the V_O concentrations, a good linear relationship was established, revealing a clear impact of V_O defects on the OER activity (Supplementary Fig. 40). However, the lower oxidation state of Ru sites and higher concentration of V_O defects were expected to result in much stronger *OH adsorption and be detrimental to the OER activity of RuO₂-based catalysts, based on the linear scaling relationships between the adsorbates binding energies following conventional AEM path^{36,81}. Accordingly, enhancement on OER activity was achieved when there were high-valent Ru sites and less V_O defects^{37,38}. This seems conflict with our result that an enhanced OER activity was obtained on V_O defects containing Zn-doped RuO₂ catalyst. We speculated that the positive effect of V_O defects on OER activity was realized with the assistance of the Zn dopants. V_O defect and Zn dopants can synergistically regulate the coordinative environment and electronic structure

of vicinal Ru centers and thus optimize the binding configurations of OER intermediates^{40,41,85}. Consequently, the OER activity may be improved.

To understand the Zn doping and oxygen vacancies effect on the OER activity, density functional theory (DFT) calculations were performed. The Zn doped RuO₂ (RuO₂:Zn) and that with O vacancies (RuO₂:Zn_V_O) were built on the optimized RuO₂ (110) surfaces (Supplementary Fig. 41). Zn was found to be more stably doped at the coordinatively unsaturated Ru (Ru_{cus}) position than the fully coordinated bridge Ru (Ru_{bri}) site, while the bridge row O could form stable vacancy site. Then, different OER paths were investigated to determine the preferred reaction pathways, including the AEM and lattice oxygen mechanism (LOM), as well as the recently highlighted dual-site oxide path mechanism (OPM) (Supplementary Fig. 42)^{35,83}. The adsorption energies of reaction intermediates were summarized in the Supplementary Table 6. For clean RuO₂, stronger binding of OH adsorbates ($\Delta G_{\text{OH}} = 0.82 \text{ eV}$) resulted in the OER proceeding favorably via a AEM path, following the four-proton-coupled electron transfer steps as H₂O → *OH → *O → *OOH → O₂³⁶. The formation of *OOH is the rate-determining step (RDS) with a large free energies barrier of 2.10 eV. By comparison, the LOM and dual site OPM paths are suppressed with much higher energy barriers of RDS (ΔG_{max} for LOM 3.79 eV and OPM 2.48 eV, where ΔG_{max} is the maximum free energy differences among the primary proton-coupled electron transfer steps) (Supplementary Fig. 43). For RuO₂_V_O, the presence of bridged O vacancies caused accumulated charge density at both the vicinal Ru_{bri} and Ru_{cus} sites (Supplementary Fig. 44), which then enhanced the binding of *OH at Ru_{cus} centers ($\Delta G_{\text{OH}} = 0.70 \text{ eV}$) and induced a larger free energies barrier of 2.28 eV for *OOH formation (Supplementary Fig. 45). Therefore, the presence of V_O defects is harmful to the OER proceeding on RuO₂^{37,38}. In contrast, on the surface of stoichiometric RuO₂:Zn oxide, the doping of Zn at Ru_{cus} sites induced a reduction of the charge density at Ru centers, which agreed with the knowledge that a fraction of the Ru will be oxidized above +4 to accommodate the divalent Zn metal³⁰. As a result, the *OH binding is weakened ($\Delta G_{\text{OH}} = 1.01 \text{ eV}$) and the OER activity is improved. More interestingly, a Ru-Zn dual-site OPM appeared to be more favorable with a lower ΔG_{max} of 1.91 eV for the third proton-coupled electron transfer step (*O_{Ru} → *O_{Ru...*}OH_{Zn}), caused by the different binding strength of intermediates on the two sites (Supplementary Fig. 46). The density of states (DOS) and charge density difference suggested that Zn donated some electron to the O and Zn had a lower *d*-band center than Ru (Fig. 5c–e). Therefore, Zn showed weaker absorption of *O, *OH, and *OOH. For example, Zn sites had a ΔG_{OH} of 1.77 eV, while Ru site had a ΔG_{OH} of 1.01 eV. This would ease the formation of second *O. In addition, the charge difference between Zn and Ru also played an important role in promoting the OER, which resulted in a -0.1 *e* charge difference for the two adsorbed *O on Zn and Ru and thus promoted the formation of O–O coupling, and eventually the formation of O₂ (Fig. 5d). With the presence of V_O defects, the charge density at both the Ru_{cus} and Zn_{cus} sites on RuO₂:Zn_V_O surface is slightly increased (Supplementary Fig. 44), associated with a shift of Ru *d*-band center away from Fermi, which further optimized the absorption of intermediates (Fig. 5e). Consequently, the ΔG_{max} (*O_{Ru} → *O_{Ru...*}OH_{Zn}) of OPM is further decreased to 1.84 eV for RuO₂:Zn with V_O defects (Fig. 5b). Therefore, we believed that the down shift of Fermi by O vacancy, the weaker absorption of *OH on Zn and the charge difference of Zn and Ru synergistically lowered the OER overpotential ($\eta = \Delta G_{\text{max}} - 1.23$) from 0.87 V for RuO₂ to 0.61 V for the O vacancy-containing Zn doped RuO₂, by converting the OER path from the single-site AEM to the dual-site OPM (Fig. 5a, b).

In terms of the stability enhancement, the present dual-site OPM path of OER avoids the step of *O → *OOH, which generally proceeds above 1.3 V on single Ru site⁸⁶. Thus, it was possible to stabilize the OER active sites against the excessive oxidation under the OPM path.

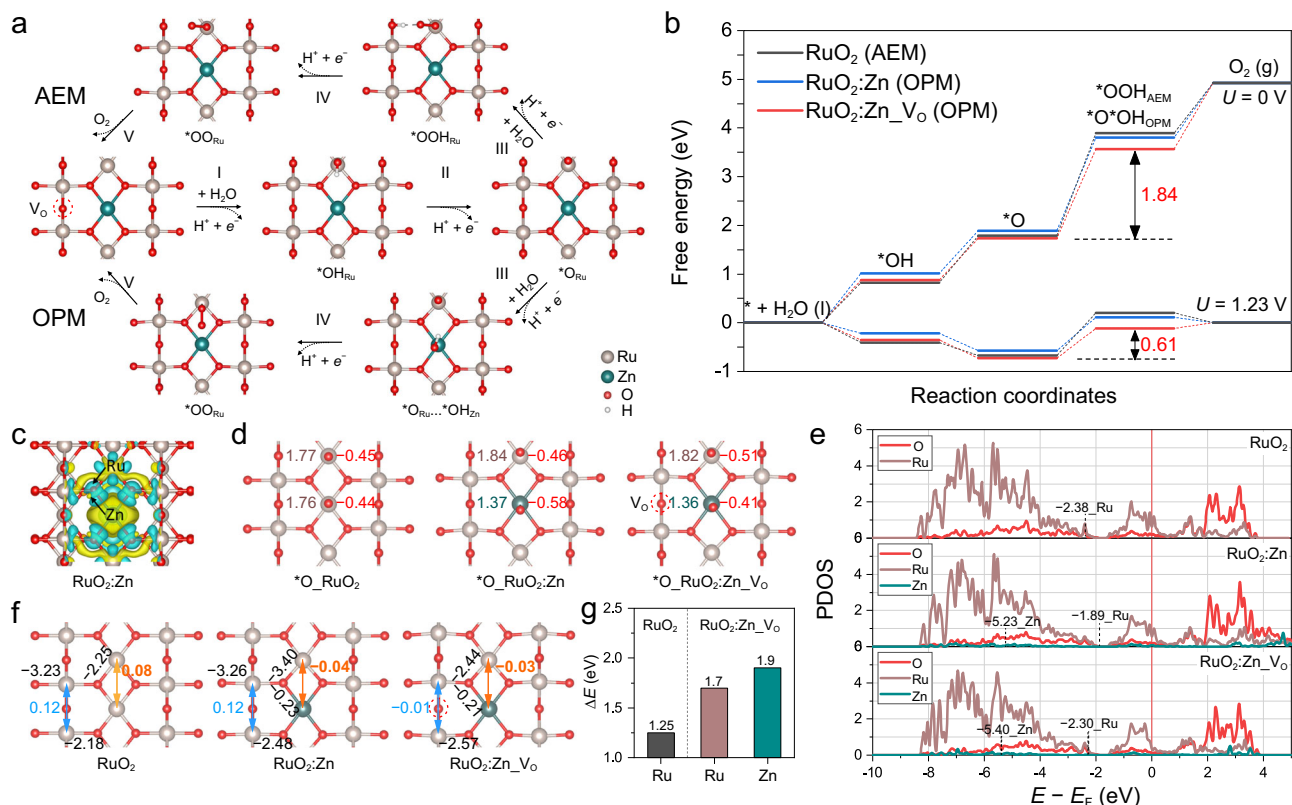


Fig. 5 | OER mechanism analysis. **a** AEM and OPM paths of OER on the RuO₂:Zn_VO surface. **b** The free energy diagrams for preferred OER paths on the surfaces of RuO₂, RuO₂:Zn, and RuO₂:Zn_VO. **c** Differential charge density analysis of RuO₂:Zn. The blue and yellow shaded area mean the electron density accumulation and donation. **d** Bader charge analysis for Ru (brown), Zn (dark cyan), and O (red) sites

on the double *O adsorbed surfaces of RuO₂, RuO₂:Zn, and RuO₂:Zn_VO. **e** PDOS of Ru 4d, O 2p, and Zn 3d-bands for RuO₂, RuO₂:Zn, and RuO₂:Zn_VO; corresponding *d*-band centers are denoted by dashed lines. **f** ICOHP analysis of Ru–O, Ru–Ru, Ru–Zn, and Zn–O on the surfaces of RuO₂, RuO₂:Zn, and RuO₂:Zn_VO. **g** De-metallization energies of Ru from RuO₂, and Ru and Zn from RuO₂:Zn_VO.

We then studied the electrochemical redox features of the Ru species on py-RuO₂:Zn, py-RuO₂, and c-RuO₂ catalysts in potential regions preceding OER process (Supplementary Fig. 47). Compared with those on py-RuO₂ and c-RuO₂, the redox peaks of Ru⁴⁺/Ruⁿ⁺ (*n* > 4) above 1.2 V were significantly suppressed on py-RuO₂:Zn, indicating an efficient protection on Ru cations from over oxidation to soluble species^{21,87,88}. Consequently, the catalytic stability of py-RuO₂:Zn for OER would be enhanced. To gain more insights into the effect of Zn doping and V_O defects on the structure stabilization of RuO₂, the crystal orbital Hamilton population (COHP) of Ru–O and Zn–O bonds, as well as Ru–Ru and Ru–Zn metal couplings, were analyzed on the optimized RuO₂, RuO₂:Zn, and RuO₂:Zn_VO surfaces. As shown in Fig. 5f, the integrated COHP (ICOHP) values of Ru_{cus}–O for RuO₂:Zn, and RuO₂:Zn_VO are –3.40 eV and –2.44 eV, respectively, which have been negatively shifted from that for pristine RuO₂ (–2.25 eV), thereby revealing a strengthened Ru_{cus}–O bond on those Zn-doped samples. In addition, small negative ICOHP values of Ru_{cus}–Zn were found on both the RuO₂:Zn (–0.04 eV) and RuO₂:Zn_VO (–0.03 eV) with the Zn doping, indicating a weak long range orbital coupling between Zn dopants and the vicinal Ru_{cus} sites. In contrast, there is no clear interaction of Ru_{cus}–Ru_{cus} (0.08 eV for ICOHP) on the pristine RuO₂. Accordingly, the Ru_{cus} sites would be further stabilized by the Zn dopants. When bridged V_O defects present, the ICOHP of Ru_{brl}–Ru_{brl} for RuO₂:Zn_VO also acquired a small negative value of –0.01 eV, while it was a positive value of 0.12 eV on both the RuO₂ and RuO₂:Zn. This indicated an enhanced interaction between two adjacent Ru_{brl} sites in the vicinity of V_O defect. The enhanced stability of Zn doped RuO₂ with V_O is also demonstrated by the de-metallization energies of Ru and Zn (Fig. 5g). The doping of Zn induced an increased de-metallization energy of Ru

by around 0.5 eV and thus stabilized the RuO₂. The Zn dopants themselves possessed relatively higher de-metallization energies by around 0.2 eV than the Ru in RuO₂:Zn_VO. The overall results suggested that the RuO₂ structure become more stable after the introduction of Zn dopants and V_O defects.

In summary, Zn-doped RuO₂ nanowire arrays with outstanding performance of acidic OER were successfully synthesized by a simple pyrolysis method. The substitutionally doping of Zn both regulated catalyst morphology and created an abundance of V_O defects and low-valent Ru sites. The self-supporting py-RuO₂:Zn nanowires (on Ti) exhibited impressive activity and durability for OER in 0.5 M H₂SO₄, evidenced by low overpotentials of 173, 304, and 373 mV at 10, 500, and 1000 mA cm^{–2}, respectively, and very modest degradations during continuous tests at 10 mA cm^{–2} for 1000 h and 50 mA cm^{–2} for 100 h. Theoretical studies showed that the V_O defects and Zn dopants caused an weakened binding of oxygen adsorbates at active Ru centers and, more interestingly, enabled a moderate adsorption of *OH species on Zn sites. As a result, the OER path was altered from the conventional AEM to a Ru–Zn dual-site OPM, thereby significantly enhancing the OER activity. In the meantime, the OPM path avoided the over oxidation of the OER metal sites and thus protected the active centers, and the presence of Zn dopants and V_O defects enabled a structure stabilization of RuO₂ matrix. Consequently, an excellent OER stability was obtained on the V_O-containing Zn-doped RuO₂ oxide.

Methods

Preparation of py-RuO₂:Zn on metallic Ti plate

Ti plate was first etched in 10 wt.% oxalic acid solution at 95 °C for 2 h to remove the surface oxide, then rinsed with copious deionized water

and dried in air. Amount of aqueous solution containing RuCl_3 and $\text{Zn}(\text{NO}_3)_2$ with controlled mole ratio of Zn/Ru and dosage of Ru^{3+} cation was pipetted onto the freshly cleaned Ti plate with a confined area of $0.5 \times 1.0 \text{ cm}^2$. The obtained precursor coating was dried naturally in air and then pyrolyzed in a muffle furnace at $350 \text{ }^\circ\text{C}$ for 4 h in air (ramping rate: $5 \text{ }^\circ\text{C min}^{-1}$) to transform the precursors to metal oxide. After naturally cooled to room temperature, the sample was then etched in 1.0 M HCl aqueous solution to remove the unwanted ZnO species. The resulted sample was rinsed with copious water and dried in air. To optimize the morphology and OER performance of py- $\text{RuO}_2\text{:Zn}$ catalyst, the conditions of preparation were screened, including the Zn/Ru mole ratio (0.2, 0.5, 1.0, 5.0) and Ru^{3+} dosage ($1.0, 3.0, 6.0 \mu\text{mol cm}^{-2}$) in the precursor solution, and the reaction temperature ($300, 350, 400, 450, 500 \text{ }^\circ\text{C}$) of pyrolysis. The results revealed that py- $\text{RuO}_2\text{:Zn}$ catalyst with regular nanowire array appearance and the best OER property can be controllably constructed under the conditions: 0.5, $6.0 \mu\text{mol cm}^{-2}$, and $350 \text{ }^\circ\text{C}$ for the Zn/Ru mole ratio, Ru^{3+} dosage, and reaction temperature, respectively.

For comparison, pure RuO_2 , referred as py- RuO_2 , was also prepared by the pyrolysis method under the optimal conditions without the addition of Zn precursor. The commercial RuO_2 , referred as c- RuO_2 , purchased from Sigma Aldrich was also used as a control sample for comparison. In addition, other materials, such as carbon fiber paper (CFP) and fluorine-doped tin oxide glass (FTO), were then used to replace the Ti plate in the fabrication of py- $\text{RuO}_2\text{:Zn}$ nanowire arrays coating under the identical conditions, in order to examine the practicability of this method on different substrates.

Physical characterizations

Scanning electron microscopic (SEM) images and energy-dispersive X-ray spectroscopy (EDS) analysis were obtained with Merlin Compact (Carl Zeiss NTS GmbH) at 15 kV. Grazing incidence XRD (GIXRD) patterns were performed on a Phillips PANalytical X'Pert Pro diffractometer operating at 40 mA and 40 kV using a curved graphite diffracted-beam monochromator with Cu $K\alpha$ radiation (incident angle = 0.3° for GIXRD, $\lambda = 1.541 \text{ \AA}$). XRD patterns were recorded by the SmartLab (Rigaku) diffractometer with Cu- $K\alpha$ radiation. High-resolution transmission electron microscopic (HRTEM) studies and high-angle annular dark-field scanning TEM (HAADF-STEM) analyses were performed on JEOL 2100 F at 200 kV. X-ray photoelectron spectroscopy (XPS) studies were carried out on Thermo ESCALAB 250XI using an Al $K\alpha$ monochromated source (150 W , $h\nu = 1486.6 \text{ eV}$). The X-ray absorption fine structure spectra (XAFS) were collected at BL14W beamline in Shanghai Synchrotron Radiation Facility (SSRF). The mass loadings of Ru and Zn in py- $\text{RuO}_2\text{:Zn}$ catalysts before and after the acid etching treatment were separately measured by ICP-MS method (Supplementary Table 1). To prepare the analytical solution, 5 mg of the py- $\text{RuO}_2\text{:Zn}$ powder scraped off the Ti substrate was dispersed in 20 mL solution containing HNO_3 , HCl , and HClO_4 with the ratio of 4:12:3, then transferred into a hydrothermal 50 mL Teflon-lined stainless-steel autoclave. Finally, the sample was sealed and treated at $180 \text{ }^\circ\text{C}$ for 72 h to fully digest all solid parts. The dissolution of Ru element was studied by inductively coupled plasma mass spectrometry (ICP-MS, Agilent 7800). Degradation of py- $\text{RuO}_2\text{:Zn}$ in duration test was monitored by taking a 1 mL sample of the electrolyte solution at different time after the test (1, 10, 50, 100, 250, 750, 1000 h) for ICP-MS analysis. The 1 mL sample was diluted with $0.5 \text{ M H}_2\text{SO}_4$ and 0.1 M HCl .

Electrochemical measurements

All electrochemical measurements were tested using a CHI 660E electrochemical analyzer (CH Instruments, Inc., Shanghai) in O_2 -saturated $0.5 \text{ M H}_2\text{SO}_4$ electrolyte. The pH of the electrolyte, 0.30 ± 0.01 , was measured with a microprocessor-based pH-meter (Leici PHSJ-3F) and further calibrated by a reversible hydrogen electrode (RHE).

A H-type three-electrode cell was used with a proton exchange membrane to separate each chamber. Saturated Ag/AgCl immersed in a double salt bridge and Pt plate served as the reference and counter electrodes, respectively. The Ag/AgCl reference electrode was first calibrated by a reversible hydrogen electrode, and the potential was reported on RHE scale with 85% iR -correction unless otherwise specified. Solution resistance ($R = 3.2 \pm 0.4, 2.9 \pm 0.4, \text{ and } 4.0 \pm 0.6 \Omega$ for py- $\text{RuO}_2\text{:Zn}$, py- RuO_2 , and c- RuO_2 , respectively) was measured by electrochemical impedance spectroscopy (EIS) at frequencies ranging from 10 Hz to 100 kHz. The current densities were calculated with respect to the geometrical area of the electrodes ($0.5 \times 1.0 \text{ cm}^2$). Linear sweep voltammetry (LSV) and cyclic voltammetry (CV) techniques were performed to examine the electrocatalytic performances of the as-prepared catalysts toward oxygen evolution reaction (OER) in acidic environments. A potential scan rate of 10 mV s^{-1} is used. Chronopotentiometric (CP) technique was employed for the long-term stability test of OER.

Density functional theory (DFT) calculations

We have employed the Vienna Ab Initio Package (VASP)^{89,90} to perform all the density functional theory (DFT) calculations within the generalized gradient approximation (GGA) using the RPBE⁹¹ formulation. We have chosen the projected augmented wave (PAW) potentials^{92,93} to describe the ionic cores and take valence electrons into account using a plane wave basis set with a kinetic energy cutoff of 450 eV. Partial occupancies of the Kohn–Sham orbitals were allowed using the Gaussian smearing method and a width of 0.05 eV. The electronic energy was considered self-consistent when the energy change was smaller than 10^{-6} eV . A 2×2 unit cell with 4-layers thickness was employed with 15 \AA vacuum in the z axis to avoid image interactions. The bottom two layers were kept fixed while the top two layers were relaxed during geometry optimization. A geometry optimization was considered convergent when the force change was smaller than 0.05 eV/\AA . Grimme's DFT-D3 methodology⁹⁴ was used to describe the dispersion interactions. The Brillouin zone integral uses the surfaces structures of $3 \times 3 \times 1$ monk horst pack K point sampling. The demetallization energies were computed as $\Delta E = E_{\text{surface}} - E_{\text{atom}} - E_{\text{surface-vac}}$, where E_{surface} and $E_{\text{surface-vac}}$ are the total energies of the surface and surfaces with one metal removed, E_{atom} is the single atom energies in the hexagonal Ru and Zn. The computational hydrogen electrode (CHE) approach was used which assumes that the chemical potential of a proton-electron pair is equal to that of gas-phase H_2 , at $U_{\text{elec}} = 0 \text{ V}$ vs. RHE. The reaction free energy of each proton-electron transfer step were obtained by $\Delta G = \Delta E + \Delta ZPE - T\Delta S + \Delta G_U + \Delta G_{\text{pH}} + \Delta G_{\text{filed}}$, where ΔE is the change in the total ground-state energy obtained from DFT calculations, ΔZPE is the change in zero-point energies, T is 298 K and ΔS is the change in entropy. $\Delta G_U = eU$, where U is the electrode potential. $\Delta G_{\text{pH}} = 0.0592 \times \text{pH}$ and the $\text{pH} = 0$ was used. ΔG_{filed} is neglected in the calculations.

Data availability

The data that support the findings of this study are available within the article and its Supplementary Information, where the source data of Figs. 1–5 are listed in the Source Data file (<https://doi.org/10.6084/m9.figshare.22621852>)⁹⁵. Extra data are available from the corresponding authors upon reasonable request. Source data are provided with this paper.

References

- Gür, T. M. Review of electrical energy storage technologies, materials and systems: challenges and prospects for large-scale grid storage. *Energy Environ. Sci.* **11**, 2696–2767 (2018).
- Li, W. et al. Exploiting Ru-induced lattice strain in CoRu nanoalloys for robust bifunctional hydrogen production. *Angew. Chem. Int. Ed.* **60**, 3290–3298 (2021).

- Song, H. et al. Single atom ruthenium-doped CoP/CDs nanosheets via splicing of carbon-dots for robust hydrogen production. *Angew. Chem. Int. Ed.* **60**, 7234–7244 (2021).
- Ding, H., Liu, H., Chu, W., Wu, C. & Xie, Y. Structural transformation of heterogeneous materials for electrocatalytic oxygen evolution reaction. *Chem. Rev.* **121**, 13174–13212 (2021).
- Ali, A., Long, F. & Shen, P. K. Innovative strategies for overall water splitting using nanostructured transition metal electrocatalysts. *Electrochem. Energy Rev.* **5**, 1 (2022).
- McCrorry, C. C. L. et al. Benchmarking hydrogen evolving reaction and oxygen evolving reaction electrocatalysts for solar water splitting devices. *J. Am. Chem. Soc.* **137**, 4347–4357 (2015).
- McCrorry, C. C. L., Jung, S., Peters, J. C. & Jaramillo, T. F. Benchmarking heterogeneous electrocatalysts for the oxygen evolution reaction. *J. Am. Chem. Soc.* **135**, 16977–16987 (2013).
- An, L. et al. Recent development of oxygen evolution electrocatalysts in acidic environment. *Adv. Mater.* **33**, 2006328 (2021).
- Lei, Z. et al. Coordination modulation of iridium single-atom catalyst maximizing water oxidation activity. *Nat. Commun.* **13**, 24 (2022).
- Chen, Z. et al. Tm Ldh meets birnessite: a 2d–2d hybrid catalyst with long-term stability for water oxidation at industrial operating conditions. *Angew. Chem. Int. Ed.* **60**, 9699–9705 (2021).
- Thangavel, P., Kim, G. & Kim, K. S. Electrochemical integration of amorphous NiFe (oxy)hydroxides on surface-activated carbon fibers for high-efficiency oxygen evolution in alkaline anion exchange membrane water electrolysis. *J. Mater. Chem. A* **9**, 14043–14051 (2021).
- He, Z. et al. Activating lattice oxygen in NiFe-based (oxy)hydroxide for water electrolysis. *Nat. Commun.* **13**, 2191 (2022).
- Carmo, M., Fritz, D. L., Mergel, J. & Stolten, D. A comprehensive review on PEM water electrolysis. *Int. J. Hydrog. Energy* **38**, 4901–4934 (2013).
- Reier, T., Nong, H. N., Teschner, D., Schlögl, R. & Strasser, P. Electrocatalytic oxygen evolution reaction in acidic environments–reaction mechanisms and catalysts. *Adv. Energy Mater.* **7**, 1601275 (2017).
- Kibsgaard, J. & Chorkendorff, I. Considerations for the scaling-up of water splitting catalysts. *Nat. Energy* **4**, 430–433 (2019).
- Chen, Z. et al. Advances in oxygen evolution electrocatalysts for proton exchange membrane water electrolyzers. *Adv. Energy Mater.* **12**, 2103670 (2022).
- Li, L., Wang, P., Shao, Q. & Huang, X. Recent progress in advanced electrocatalyst design for acidic oxygen evolution reaction. *Adv. Mater.* **33**, 2004243 (2021).
- She, L. et al. On the durability of iridium-based electrocatalysts toward the oxygen evolution reaction under acid environment. *Adv. Funct. Mater.* **32**, 2108465 (2022).
- Spöri, C., Kwan, J. T. H., Bonakdarpour, A., Wilkinson, D. P. & Strasser, P. The stability challenges of oxygen evolving catalysts: towards a common fundamental understanding and mitigation of catalyst degradation. *Angew. Chem. Int. Ed.* **56**, 5994–6021 (2017).
- Roy, C. et al. Trends in activity and dissolution on RuO₂ under oxygen evolution conditions: particles versus well-defined extended surfaces. *ACS Energy Lett.* **3**, 2045–2051 (2018).
- Rao, R. R. et al. Operando identification of site-dependent water oxidation activity on ruthenium dioxide single-crystal surfaces. *Nat. Catal.* **3**, 516–525 (2020).
- Scott, S. B. et al. The low overpotential regime of acidic water oxidation part ii: trends in metal and oxygen stability numbers. *Energy Environ. Sci.* **15**, 1988–2001 (2022).
- Chen, F.-Y., Wu, Z.-Y., Adler, Z. & Wang, H. Stability challenges of electrocatalytic oxygen evolution reaction: from mechanistic understanding to reactor design. *Joule* **5**, 1704–1731 (2021).
- Sun, H. & Jung, W. Recent advances in doped ruthenium oxides as high-efficiency electrocatalysts for the oxygen evolution reaction. *J. Mater. Chem. A* **9**, 15506–15521 (2021).
- Harzandi, A. M. et al. Ruthenium core–shell engineering with nickel single atoms for selective oxygen evolution via nondestructive mechanism. *Adv. Energy Mater.* **11**, 2003448 (2021).
- Wang, J. et al. Single-site Pt-doped RuO₂ hollow nanospheres with interstitial C for high-performance acidic overall water splitting. *Sci. Adv.* **8**, eabl9271 (2022).
- Chen, S. et al. Mn-doped RuO₂ nanocrystals as highly active electrocatalysts for enhanced oxygen evolution in acidic media. *ACS Catal.* **10**, 1152–1160 (2020).
- Su, J. et al. Assembling ultrasmall copper-doped ruthenium oxide nanocrystals into hollow porous polyhedra: highly robust electrocatalysts for oxygen evolution in acidic media. *Adv. Mater.* **30**, 1801351 (2018).
- Retuerto, M. et al. Na-doped ruthenium perovskite electrocatalysts with improved oxygen evolution activity and durability in acidic media. *Nat. Commun.* **10**, 2041 (2019).
- Burnett, D. L. et al. (M,Ru)O₂ (M = Mg, Zn, Cu, Ni, Co) rutiles and their use as oxygen evolution electrocatalysts in membrane electrode assemblies under acidic conditions. *Chem. Mater.* **32**, 6150–6160 (2020).
- Wang, K. et al. Highly active ruthenium sites stabilized by modulating electron-feeding for sustainable acidic oxygen-evolution electrocatalysis. *Energy Environ. Sci.* **15**, 2356–2365 (2022).
- Zhou, C. et al. Superdurable bifunctional oxygen electrocatalyst for high-performance zinc–air batteries. *J. Am. Chem. Soc.* **144**, 2694–2704 (2022).
- Hao, S. et al. Dopants fixation of ruthenium for boosting acidic oxygen evolution stability and activity. *Nat. Commun.* **11**, 5368 (2020).
- Wang, X. et al. Electronic structure modulation of RuO₂ by TiO₂ enriched with oxygen vacancies to boost acidic O₂ evolution. *ACS Catal.* **12**, 9437–9445 (2022).
- Lin, C. et al. In-situ reconstructed Ru atom array on α -MnO₂ with enhanced performance for acidic water oxidation. *Nat. Catal.* **4**, 1012–1023 (2021).
- Man, I. C. et al. Universality in oxygen evolution electrocatalysis on oxide surfaces. *ChemCatChem* **3**, 1159–1165 (2011).
- Gayen, P., Saha, S., Bhattacharyya, K. & Ramani, V. K. Oxidation state and oxygen-vacancy-induced work function controls bifunctional oxygen electrocatalytic activity. *ACS Catal.* **10**, 7734–7746 (2020).
- Hubert, M. A. et al. Acidic oxygen evolution reaction activity–stability relationships in Ru-based pyrochlores. *ACS Catal.* **10**, 12182–12196 (2020).
- Dickens, C. F. & Nørskov, J. K. A theoretical investigation into the role of surface defects for oxygen evolution on RuO₂. *J. Phys. Chem. C* **121**, 18516–18524 (2017).
- Zhang, L. et al. Sodium-decorated amorphous/crystalline RuO₂ with rich oxygen vacancies: a robust pH-universal oxygen evolution electrocatalyst. *Angew. Chem. Int. Ed.* **60**, 18821–18829 (2021).
- Qin, Y. et al. RuO₂ electronic structure and lattice strain dual engineering for enhanced acidic oxygen evolution reaction performance. *Nat. Commun.* **13**, 3784 (2022).
- Kuznetsov, D. A. et al. Tailoring lattice oxygen binding in ruthenium pyrochlores to enhance oxygen evolution activity. *J. Am. Chem. Soc.* **142**, 7883–7888 (2020).
- Seh, Z. W. et al. Combining theory and experiment in electrocatalysis: insights into materials design. *Science* **355**, 146 (2017).
- Zhao, Z. L. et al. Boosting oxygen evolution reaction using defect-rich ultra-thin ruthenium oxide nanosheets in acidic media. *Energy Environ. Sci.* **13**, 5143–5151 (2020).

45. Ge, R. et al. Ultrafine defective RuO₂ electrocatalyst integrated on carbon cloth for robust water oxidation in acidic media. *Adv. Energy Mater.* **9**, 1901313 (2019).
46. Sun, H. et al. Self-supported transition-metal-based electrocatalysts for hydrogen and oxygen evolution. *Adv. Mater.* **32**, 1806326 (2020).
47. Karlsson, R. K. B. & Cornell, A. Selectivity between oxygen and chlorine evolution in the chlor-alkali and chlorate processes. *Chem. Rev.* **116**, 2982–3028 (2016).
48. Petrykin, V. et al. Zn-doped RuO₂ electrocatalysts for selective oxygen evolution: relationship between local structure and electrocatalytic behavior in chloride containing media. *Chem. Mater.* **23**, 200–207 (2011).
49. Shannon, R. D. & Prewitt, C. T. Effective ionic radii in oxides and fluorides. *Acta Crystallogr. B* **25**, 925–946 (1969).
50. Chueh, Y. L. et al. RuO₂ nanowires and RuO₂/TiO₂ core/shell nanowires: from synthesis to mechanical, optical, electrical, and photoconductive properties. *Adv. Mater.* **19**, 143–149 (2007).
51. Kang, M. et al. Single carbon fiber decorated with RuO₂ nanorods as a highly electrocatalytic sensing element. *Anal. Chem.* **84**, 9485–9491 (2012).
52. Chen, Z. G., Pei, F., Pei, Y. T. & De Hosson, J. T. M. A versatile route for the synthesis of single crystalline oxide nanorods: growth behavior and field emission characteristics. *Cryst. Growth Des.* **10**, 2585–2590 (2010).
53. Lee, Y. et al. Facile synthesis of single crystalline metallic RuO₂ nanowires and electromigration-induced transport properties. *J. Phys. Chem. C* **115**, 4611–4615 (2011).
54. Kuete Saa, D. et al. Synthesis of RuO₂ nanowires from Ru thin films by atmospheric pressure micro-post-discharge. *Surf. Coat. Technol.* **295**, 13–19 (2016).
55. Lin, S. et al. Ni–Zn dual sites switch the CO₂ hydrogenation selectivity via tuning of the *d*-band center. *ACS Catal.* **12**, 3346–3356 (2022).
56. Katea, S. N., Broqvist, P., Kullgren, J., Hemmer, E. & Westin, G. Fast, low-cost synthesis of ZnO:Eu nanosponges and the nature of In doping in ZnO. *Inorg. Chem.* **59**, 7584–7602 (2020).
57. Liu, B. & Zeng, H. C. Fabrication of ZnO “dandelions” via a modified kirkendall process. *J. Am. Chem. Soc.* **126**, 16744–16746 (2004).
58. Morgan, D. J. Resolving ruthenium: XPS studies of common ruthenium materials. *Surf. Interface Anal.* **47**, 1072–1079 (2015).
59. Karlsson, R. K. B., Cornell, A. & Pettersson, L. G. M. Structural changes in RuO₂ during electrochemical hydrogen evolution. *J. Phys. Chem. C* **120**, 7094–7102 (2016).
60. Chen, Y. et al. A robust fuel cell operated on nearly dry methane at 500 °C enabled by synergistic thermal catalysis and electrocatalysis. *Nat. Energy* **3**, 1042–1050 (2018).
61. Doubova, L. M., Daolio, S. & De Battisti, A. Examination of RuO₂ single-crystal surfaces: charge storage mechanism in H₂SO₄ aqueous solution. *J. Electroanal. Chem.* **532**, 25–33 (2002).
62. Arikawa, T., Takasu, Y., Murakami, Y., Asakura, K. & Iwasawa, Y. Characterization of the structure of RuO₂–IrO₂/Ti electrodes by exafs. *J. Phys. Chem. B* **102**, 3736–3741 (1998).
63. Liu, Y. et al. Enhanced N₂ electroreduction over LaCoO₃ by introducing oxygen vacancies. *ACS Catal.* **10**, 1077–1085 (2020).
64. Li, P. et al. Visible-light-driven nitrogen fixation catalyzed by Bi₅O₇Br nanostructures: enhanced performance by oxygen vacancies. *J. Am. Chem. Soc.* **142**, 12430–12439 (2020).
65. Peng, S. et al. Necklace-like multishelled hollow spinel oxides with oxygen vacancies for efficient water electrolysis. *J. Am. Chem. Soc.* **140**, 13644–13653 (2018).
66. Jeon, H. S. et al. Operando evolution of the structure and oxidation state of size-controlled Zn nanoparticles during CO₂ electroreduction. *J. Am. Chem. Soc.* **140**, 9383–9386 (2018).
67. Ozkendir, O. M., Yildirimcan, S., Yuzer, A. & Ocakoglu, K. Crystal and electronic structure study of Mn doped wurtzite ZnO nanoparticles. *Prog. Nat. Sci. Mater. Int.* **26**, 347–353 (2016).
68. Lin, Y. et al. Chromium-ruthenium oxide solid solution electrocatalyst for highly efficient oxygen evolution reaction in acidic media. *Nat. Commun.* **10**, 162 (2019).
69. Wang, Y. et al. Structurally disordered RuO₂ nanosheets with rich oxygen vacancies for enhanced nitrate electroreduction to ammonia. *Angew. Chem. Int. Ed.* **61**, e202202604 (2022).
70. Wei, C. et al. Recommended practices and benchmark activity for hydrogen and oxygen electrocatalysis in water splitting and fuel cells. *Adv. Mater.* **31**, 1806296 (2019).
71. Zhao, S., Yang, Y. & Tang, Z. Insight into structural evolution, active sites, and stability of heterogeneous electrocatalysts. *Angew. Chem. Int. Ed.* **61**, e202110186 (2022).
72. Stoerzinger, K. A., Qiao, L., Biegalski, M. D. & Shao-Horn, Y. Orientation-dependent oxygen evolution activities of rutile IrO₂ and RuO₂. *J. Phys. Chem. Lett.* **5**, 1636–1641 (2014).
73. Wen, Y. et al. Stabilizing highly active Ru sites by suppressing lattice oxygen participation in acidic water oxidation. *J. Am. Chem. Soc.* **143**, 6482–6490 (2021).
74. Zhang, H., Wu, B., Su, J., Zhao, K. & Chen, L. MOF-derived zinc-doped ruthenium oxide hollow nanorods as highly active and stable electrocatalysts for oxygen evolution in acidic media. *ChemNano-Mat* **7**, 117–121 (2021).
75. Zhou, Y.-N. et al. Surface evolution of Zn doped-RuO₂ under different etching methods towards acidic oxygen evolution. *J. Mater. Chem. A* **10**, 16193–16203 (2022).
76. Anantharaj, S., Noda, S., Driess, M. & Menezes, P. W. The pitfalls of using potentiodynamic polarization curves for tafel analysis in electrocatalytic water splitting. *ACS Energy Lett.* **6**, 1607–1611 (2021).
77. Dickens, C. F., Kirk, C. & Nørskov, J. K. Insights into the electrochemical oxygen evolution reaction with ab initio calculations and microkinetic modeling: Beyond the limiting potential volcano. *J. Phys. Chem. C* **123**, 18960–18977 (2019).
78. Geiger, S. et al. The stability number as a metric for electrocatalyst stability benchmarking. *Nat. Catal.* **1**, 508–515 (2018).
79. Cherevko, S. et al. Oxygen and hydrogen evolution reactions on Ru, RuO₂, Ir, and IrO₂ thin film electrodes in acidic and alkaline electrolytes: a comparative study on activity and stability. *Catal. Today* **262**, 170–180 (2016).
80. Wang, Z., Guo, X., Montoya, J. & Nørskov, J. K. Predicting aqueous stability of solid with computed pourbaix diagram using scan functional. *NPJ Comput. Mater.* **6**, 160 (2020).
81. Rossmeisl, J., Qu, Z. W., Zhu, H., Kroes, G. J. & Nørskov, J. K. Electrolysis of water on oxide surfaces. *J. Electroanal. Chem.* **607**, 83–89 (2007).
82. Scott, S. B. et al. The low overpotential regime of acidic water oxidation part I: the importance of O₂ detection. *Energy Environ. Sci.* **15**, 1977–1987 (2022).
83. Vonrüti, N., Rao, R., Giordano, L., Shao-Horn, Y. & Aschauer, U. Implications of nonelectrochemical reaction steps on the oxygen evolution reaction: oxygen dimer formation on perovskite oxide and oxynitride surfaces. *ACS Catal.* **12**, 1433–1442 (2022).
84. Zhu, K., Shi, F., Zhu, X. & Yang, W. The roles of oxygen vacancies in electrocatalytic oxygen evolution reaction. *Nano Energy* **73**, 104761 (2020).
85. Jin, H. et al. Safeguarding the RuO₂ phase against lattice oxygen oxidation during acidic water electrooxidation. *Energy Environ. Sci.* **15**, 1119–1130 (2022).
86. Rao, R. R. et al. Towards identifying the active sites on RuO₂(110) in catalyzing oxygen evolution. *Energy Environ. Sci.* **10**, 2626–2637 (2017).

87. Stoerzinger, K. A. et al. Orientation-dependent oxygen evolution on RuO₂ without lattice exchange. *ACS Energy Lett.* **2**, 876–881 (2017).
88. Guerrini, E., Consonni, V. & Trasatti, S. Surface and electrocatalytic properties of well-defined and vicinal RuO₂ single crystal faces. *J. Solid State Electrochem.* **9**, 320–329 (2005).
89. Kresse, G. & Furthmüller, J. Efficient iterative schemes for ab initio total-energy calculations using a plane-wave basis set. *Phys. Rev. B* **54**, 11169–11186 (1996).
90. Perdew, J. P., Burke, K. & Ernzerhof, M. Generalized gradient approximation made simple. *Phys. Rev. Lett.* **77**, 3865–3868 (1996).
91. Hammer, B., Hansen, L. B. & Nørskov, J. K. Improved adsorption energetics within density-functional theory using revised perdue-burke-ernzerhof functionals. *Phys. Rev. B* **59**, 7413–7421 (1999).
92. Grimme, S., Antony, J., Ehrlich, S. & Krieg, H. A consistent and accurate ab initio parametrization of density functional dispersion correction (DFT-D) for the 94 elements H-Pu. *J. Chem. Phys.* **132**, 154104 (2010).
93. Blöchl, P. E. Projector augmented-wave method. *Phys. Rev. B* **50**, 17953–17979 (1994).
94. Henkelman, G., Uberuaga, B. P. & Jónsson, H. A climbing image nudged elastic band method for finding saddle points and minimum energy paths. *J. Chem. Phys.* **113**, 9901–9904 (2000).
95. Zhang, D. et al. Construction of Zn-doped RuO₂ nanowires for exceptional efficient and stable water oxidation in acidic media. *figshare. Dataset* <https://doi.org/10.6084/m9.figshare.22621852> (2023).

Acknowledgements

The authors would like to acknowledge financial supports from the Natural Science Foundation of Henan Province (182300410196), National Natural Science Foundation of China (U22A20120, 52071135, 51871090, U1804135, and 51671080), Plan for Scientific Innovation Talent of Henan Province (194200510019), and Key Project of Educational Commission of Henan Province (19A150025).

Author contributions

D.Z., B.L., and S.L. conceived the study. M.L., Y.Y., B.X., and D.Z. designed the experiment and performed the initial tests. X.Y. conducted the theoretical calculations. H.S., and G.I.N.W. assisted in the data

analysis. D.Z., M.L., and X.Y. co-wrote the manuscript. All authors discussed the results and commented on the manuscript.

Competing interests

The authors declare no competing interests.

Additional information

Supplementary information The online version contains supplementary material available at <https://doi.org/10.1038/s41467-023-38213-1>.

Correspondence and requests for materials should be addressed to Baozhong Liu or Siyu Lu.

Peer review information *Nature Communications* thanks Maria Retuerto, Michal Bajdich and the other anonymous reviewer(s) for their contribution to the peer review of this work. Peer review reports are available.

Reprints and permissions information is available at <http://www.nature.com/reprints>

Publisher's note Springer Nature remains neutral with regard to jurisdictional claims in published maps and institutional affiliations.

Open Access This article is licensed under a Creative Commons Attribution 4.0 International License, which permits use, sharing, adaptation, distribution and reproduction in any medium or format, as long as you give appropriate credit to the original author(s) and the source, provide a link to the Creative Commons license, and indicate if changes were made. The images or other third party material in this article are included in the article's Creative Commons license, unless indicated otherwise in a credit line to the material. If material is not included in the article's Creative Commons license and your intended use is not permitted by statutory regulation or exceeds the permitted use, you will need to obtain permission directly from the copyright holder. To view a copy of this license, visit <http://creativecommons.org/licenses/by/4.0/>.

© The Author(s) 2023